[Article Full Title]
Respiratory-correlated Four-dimensional Magnetic Resonance Fingerprinting (RC-4DMRF) for Liver Cancer Radiotherapy Motion Management

[Short Running Title]

RC-4DMRF for liver cancer radiotherapy

[Author Names]
Chenyang LIU[1], Tian LI[1], Peng CAO[2], Edward S. HUI[3,4], Yat-Lam WONG[1], Zuojun WANG[2], Haonan XIAO[1], Shaohua ZHI[1], Ta ZHOU[1], Wen LI[1], Sai Kit LAM[5,6], Andy Lai-yin CHEUNG[7], Victor Ho-fun LEE[8], Michael YING [1]*, Jing CAI[1,6]*

*Authors to whom correspondence should be addressed.

[Author Institutions]
[1] Department of Health Technology and Informatics, The Hong Kong Polytechnic University, Hong Kong SAR, 999077, China

[2] Department of Diagnostic Radiology, The University of Hong Kong, Hong Kong SAR, 999077, China

[3] Department of Imaging and Interventional Radiology, The Chinese University of Hong Kong, Hong Kong SAR, 999077, China

[4] Department of Psychiatry, The Chinese University of Hong Kong, Hong Kong SAR, 999077, China

[5] Department of Biomedical Engineering, The Hong Kong Polytechnic University, Hong Kong SAR, 999077, China

[6] Research Institute for Smart Ageing, The Hong Kong Polytechnic University, Hong Kong SAR, 999077, China

[7] Department of Clinical Oncology, Queen Mary Hospital, Hong Kong SAR, 999077, China

[8] Department of Clinical Oncology, The University of Hong Kong, Hong Kong SAR, 999077, China

[Corresponding Author Name & Email Address]
Jing CAI, corresponding author

jing.cai@polyu.edu.hk

Department of Health Technology and Informatics, The Hong Kong Polytechnic University, Hung Hom, Kowloon, Hong Kong

Michael YING, co-corresponding author

michael.ying@polyu.edu.hk

Department of Health Technology and Informatics, The Hong Kong Polytechnic University, Hung Hom, Kowloon, Hong Kong

[Author Responsible for Statistical Analysis Name & Email Address]

Chenyang Liu

chenyang.liu@connect.polyu.hk

Department of Health Technology and Informatics, The Hong Kong Polytechnic University, Hung Hom, Kowloon, Hong Kong

[Conflict of Interest Statement for All Authors]

Conflict of Interest: None

[Funding Statement]

This research was partly supported by General Research Funds (GRF 15102219, GRF 15104822), National Natural Science Foundation of China (NSFC) Young Scientist Fund (82202941), Natural Science Foundation of Jiangsu Province (BK20191200), Natural Science Fund for Colleges and Universities in Jiangsu Province (19JKD520003), Postgraduate Research & Practice Innovation Program of Jiangsu Province (KYCX21_3506, KYCX_3825), and a research studentship of the Hong Kong Polytechnic University (RKWF).

[Data Availability Statement for this Work]

Research data is not available at this time.

[Acknowledgements]

None

Abstract

Purpose: To develop a respiratory-correlated four-dimensional imaging technique based on magnetic resonance fingerprinting (MRF), i.e., RC-4DMRF, for liver tumor motion management in radiotherapy.

Methods: Thirteen liver cancer patients were prospectively enrolled in this study. *k*-space MRF signals of the liver were acquired during free-breathing using the FISP sequence on a 3T scanner. The signals were binned into eight respiratory phases based on respiratory surrogates, and inter-phase displacement vector fields (DVFs) were estimated using a phase-specific low-rank optimization method. Hereafter, the tissue property maps, including T1 and T2 relaxation times, and proton density (PD), were reconstructed using a pyramid motion-compensated method that alternatively optimized inter-phase DVFs and subspace images. To evaluate the efficacy of RC-4DMRF, amplitude motion differences (AMDs) and Pearson correlation coefficients (PCCs) were determined to assess measurement agreement in tumor motion between RC-4DMRF and cine MRI; mean absolute percentage errors (MAPEs) of the RC-4DMRF-derived tissue maps were calculated to reveal tissue quantification accuracy using digital human phantom; tumor-to-liver contrast-to-noise ratio (CNR) of RC-4DMRF images was compared with that of planning CT and contrast-enhanced MRI (CE-MRI) images. Paired Student's t-test was used for statistical significance analysis with a p-value threshold of 0.05.

Results: RC-4DMRF achieved excellent agreement in motion measurement with cine MRI, yielding the mean (± standard deviation) PCCs of 0.95±0.05 and 0.93±0.09 and AMDs of 1.48±1.06 mm and 0.81±0.64 mm in the superior-inferior and anterior-posterior directions, respectively. Moreover, RC-4DMRF achieved high accuracy in tissue property quantification, with MAPEs of 8.8%, 9.6%, and 5.0% for T1, T2, and PD, respectively. Notably, the tumor CNR

in RC-4DMRI-derived T1 maps (6.41±3.37) was found to be the highest among all tissue property maps, approximately equal to that of CE-MRI (6.96±1.01, p-value=0.862), and substantially higher than that of planning CT (2.91±1.97, p-value=0.048).

Conclusion: RC-4DMRF demonstrated high accuracy in respiratory motion measurement and tissue properties quantification, potentially facilitating tumor motion management in liver radiotherapy.

1 Introduction

Liver cancer is a devastating malignancy threatening millions of lives worldwide [1, 2]. Radiotherapy (RT) is an indispensable therapeutic modality in the treatment of liver cancer. However, achieving precise radiation dose coverage to liver tumors is practically challenging because of respiratory motion, where the liver may move up to 40-50 mm during normal breathing [3, 4]. If not properly managed, the respiratory motion may incur unnecessary radiation-induced liver toxicity and treatment failure [5]. In recent years, four-dimentional magnetic resonance imaging (4DMRI) has emerged as a promising technique for respiratory motion management. This non-invasive imaging method provides comprehensive tumor/organ motion information throughout the breathing cycle, with excellent discrimination between tumor and healthy tissues [6-10]. Despite its potential benefits, current 4DMRI techniques have several limitations, especially the inter-patient tumor contrast inconsistency and insufficient temporal resolution, which can compromise the accuracy of motion management and limit its widespread clinical application.

+

Several preliminary 4DMRF methods have been developed using retrospective reconstruction [11-15]. In these methods, free-breathing MRF signals are correlated with respiratory surrogates and are retrospectively binned into multiple respiratory motion phases. Hereafter, the MRF images of each phase are independently reconstructed. The retrospective reconstruction may lead to a deterioration in image quality due to a reduction in the number of *k*-space signals available per motion phase. Li *et al*. addressed this problem by using 10 repeated MRF scans to acquire sufficient MRF signals for each motion phase [11]. However, the scan time is prohibitively long (~3 mins for a two-dimensional (2D) slice), diminishing the popularity of this

approach in clinical applications. Huang *et al*. devised a comparable approach that bins signals into only two phases, resulting in a reduced scan time but at the cost of compromised temporal resolution [13]. Recently, motion compensation (MC) has been used to substantially decrease scan time in 4DMRF by more than fivefold [14, 15]. Following retrospective binning, MC methods calculate the displacement vector fields (DVFs) to capture the inter-phase motion pattern between each pair of respiratory phases. These MC methods obtain sufficient data by deforming MRF dynamics from the other phases to the target phase, rather than by conducting repeated MRF scans. Building on this approach, Cruz *et al*. [14] used the alternating direction method of multipliers to reconstruct motion-resolved tissue maps, while Cao *et al*. [15] developed a sliding-window approach to calculate inter-phase DVFs.

Despite the abovementioned efforts to develop the 4DMRF technique, it remains unready for clinical implementation in RT because of the following limitations. First, the temporal resolutions of current 4DMRF methods are insufficient to enable their application in RT. For instance, only two [13] and three [14] respiratory phases have been reported, whereas eight to ten phases are commonly required for RT in clinical practice. Second, the accuracy of quantitative tissue mapping offered by current 4DMRF methods is suboptimal. This occurs because reference images used for motion calculation have significant under-sampling artifacts, which decreases the accuracy of DVF calculations, leading to inaccurate tissue mapping [15]. Third, current 4DMRF methods were developed and tested on healthy volunteers, and the clinical validation of these methods for patients with liver cancer remains unanswered.

Accordingly, in the present study, a novel respiratory-correlated 4DMRF (RC-4DMRF) technique was developed for tumor motion management in liver cancer RT. This technique innovatively integrates a pyramid motion-compensation design that substantially increases the

accuracy of 4DMRF reconstruction. Notably, this study represents the first-of-its-kind to demonstrate the 4DMRF performance on liver cancer patients. The effectiveness of this technique was evaluated in aspects of tumor motion measurement accuracy, tissue quantification accuracy, and tumor-to-liver contrast-noise-ratio (CNR) in order to demonstrate its feasibility for clinical implementation, for the first time, for liver cancer. Results of the present work would lay a foundation for applying RC-4DMRF in RT of liver cancer, including but not limited to accurate target volume determination and inter-fraction motion assessment.

2 Methods and Materials

2.1 RC-4DMRF image reconstruction

The MRF reconstruction pipeline process typically involves three key stages, namely, signal acquisition, dictionary simulation, and pattern matching, which have been explicitly introduced in previous studies [16-19]. The signal acquisition stage involves acquiring *k*-space signals at each TR (i.e., each time position) and reconstructing the corresponding MRF dynamics using Fourier transform. In the dictionary simulation stage, a lookup table is constructed based on MRF scan parameters (e.g., FAs and TRs) using a Bloch equation [20], which contains the theoretical fingerprints of various tissue types and their respective tissue property values (e.g., T1, T2, and PD). Finally, in the pattern matching stage, the reconstructed MRF dynamics are compared voxel-by-voxel with the lookup table to determine the tissue values. Dot-product is performed between measured fingerprints with theoretical fingerprints, and the best-fitting tissue property values are retrieved by exhaustively searching the maximum dot-product values [19]. Furthermore, the time-series MRF dynamics demonstrate low-rank compressibility in the time dimension [21]. This property facilitates the derivation of a low-rank subspace basis from the dictionary, leading

to the creation of a low-rank dictionary. By projecting the full-rank MRF dynamics onto the subspace basis, the MRF dynamics are transformed into multiple subspace images. The pattern matching process is then performed between the low-rank subspace images and the low-rank dictionary. The utilization of the low-rank property of MRF in reconstruction has been shown to effectively reduce computational burdens and improve reconstruction accuracies [17, 18].

RC-4DMRF integrates two novel components, namely initial inter-phase motion estimation and pyramid motion-compensated optimization, into the MRF reconstruction pipeline to address the challenge of respiratory motion. A schematic illustration of the RC-4DMRF algorithm is shown in **Figure 1**. Initial inter-phase motion estimation utilizes a phase-specific low-rank optimization (PS-LR-O) method to estimate inter-phase DVFs from *k*-space MRF signals corrupted by motion artifacts **(Figure 1(a)**). The second component, pyramid motion-compensated optimization, optimizes the subspace images and inter-phase DVFs using an alternative minimization strategy, with the estimated inter-phase DVFs from the former component as input (**Figure 1(b)**). A final pattern matching step is performed on the optimized subspace images to produce the tissue maps of each phase. Details of initial inter-phase motion estimation and pyramid motion-compensated optimization are described in the following subsections.

2.1.1 Initial inter-phase motion estimation

Free-breathing MRF signals are first binned into eight motion phases based on respiratory surrogates (**Figure 1(a), left**), and inter-phase DVFs are then estimated from the subspace images derived from PS-LR-O (**Figure 1(a), right**).

PS-LR-O is a low-rank-based method that employs total variation (TV) regularization to reduce under-sampling artifacts and noise of subspaces images. The PS-LR-O method projects

binned raw *k*-space signals to subspace images by singular value decomposition and optimizes the subspace images of each phase *i* independently using the l2-norm function defined in **Equation (1)**,

$$arg\min_{x_i}\|\mathcal{F}_i x_i - \mathcal{P}_i y\|_2^2 + \lambda\|TV\|_1, \text{ for } i = 1, \dots, 8 \quad (1)$$

where $\mathcal{F}_i$ is the low-rank non-uniform fast Fourier transform (NUFFT) operator of phase *i* [18], which combines the Fourier transform matrix and the low-rank projection matrix into a single matrix to reduce the computational burden [17], and is constructed based on the *k*-space trajectory at the dynamic position of phase *i*; x_i is the low-rank subspace image of phase *i*; *y* is the raw *k*-space data; and $\mathcal{P}_i$ is a phase-binning operator that retains only the *k*-space data belonging to phase *i*. Five ranks are used in the optimization, and the TV regularization is applied to the spatial dimension to enforce the sparsity of the subspace images. **Equation (1)** is solved by non-linear conjugate gradient (CG) descent [22] with a regularization weight (λ) of 0.002 and a fixed iteration step of 10.

The main subspace images represent the principal anatomical structure of each phase, and the inter-phase DVFs are calculated based on them. Because the contrast of the main subspace images varies between phases, DVFs are calculated using a free-form registration algorithm that employs mutual information as a cost function [23-25]. This algorithm calculates B-spline deformation at various image resolutions using the following parameters: histogram bins of 50, a gridding size of 15 pixels, and a maximum of 1,000 iterations at each resolution level.

The respiratory signals of MRF data are determined from MRF dynamics using a sliding-window approach [26]. Specifically, a series of sliding-window images are obtained by combining consecutive MRF dynamics within a finite acquisition time window (~0.01 s). The respiratory

amplitudes are determined by the diaphragm positions from the sliding window images by a self-developed edge-detection algorithm.

2.1.2 Pyramid motion-compensated optimization

Section 2.1.1 describes the utilization of phase-specific *k*-space signals for optimizing the subspace images of each phase. However, despite their sufficiency for inter-phase motion estimation, these subspace images do not contain adequate information for pattern matching because of phase sorting-induced reduction in MRF dynamics. Therefore, to improve the subspace images of each phase, pyramid motion-compensated optimization was developed, as illustrated in **Figure 1(b)**, consisting of a subspace image optimization branch (indicated by the blue arrows) and a DVF optimization branch (indicated by the yellow arrows).

The optimization of subspace images is achieved via a motion compensation design, with the assistance of the calculated DVFs, as formulated in **Equation (2)**,

$$arg\min_{x_i}\left\|\sum_{p=1}^{8}\mathcal{A}_p\mathcal{F}\,\mathcal{M}_i^p x_i - y\right\|_2^2 + \lambda\|TV\|_1, \text{ for } i = 1, \dots, 8 \qquad (2)$$

where $\mathcal{A}_p$ is the *k*-space sampling operator and represents a list of binary masks that equal 1 when the TR position belongs to phase *p* and 0 otherwise; $\mathcal{F}$ is the low-rank NUFFT operator constructed based on the *k*-space trajectory from all of the dynamics, which is different from the $\mathcal{F}_i$ used in **Equation (1)** that utilizes phase-specific *k*-space trajectory; $\mathcal{M}_i^p$ is the DVF between the phase p and the target phase i; and x_i represents the subspace images of the target phase *i*. **Equation (2)** is solved iteratively using non-linear CG descent. As shown in **Figure 1(b)**, the forward iteration can be regarded as an approximation of the *k*-space MRF data (y) from the subspace images of the target phase (x_i) and the DVFs between the target phase and other phases ($\mathcal{M}_i^1$,…, $\mathcal{M}_i^8$). First, the subspace images of the target phase (x_i) are deformed to other phases using the calculated DVFs,

thereby obtaining subspace images of all eight phases. Subsequently, a forward low-rank NUFFT operation ($\mathcal{F}$) is implemented on these deformed subspace images to obtain *k*-space data for each phase. The generated *k*-space data are subjected to *k*-space sampling ($\mathcal{A}_1, \ldots, \mathcal{A}_8$) to mask the *k*-space data that do not belong to the deformed phases. The generated *k*-space signals of each phase are then combined via a summation operation, and the resulting combined *k*-space data are compared with the raw MRF signals (y). The backward process, on the other hand, performs the calculation in the opposite direction, i.e., deforms the *k*-space residual back to the subspace images [27]. The initial inputs of **Equation (2)** include the DVFs estimated in **Section 2.1.1** ($\mathcal{M}^{[0]}$) and zeros-valued subspace images ($x_i^{[0]}$). The error between the calculated *k*-space data and raw data is iteratively minimized using a fixed iteration of 20. An early-stopping criterion is used if the optimization converges. **Equation (2)** applies a TV constraint in the spatial dimension with a regularization weight of 0.002.

The optimization of the DVFs is performed on the optimized subspace images and is repeated three times via an alternative optimization approach. The optimized subspace images mitigate under-sampling artifacts and noises, providing an improved image quality for inter-phase DVF calculation. Therefore, after the subspace images are optimized for all of the motion phases, the inter-phase DVFs are recalculated using the registration algorithm described in **Section 2.1.1**. The resulting updated DVFs, in return, improve the spatial accuracy in the subspace image. A pyramid registration method was developed for the three DVF optimization iteration steps: the initial iterations focus on large-scale motion, whereas the later iterations focus on refined structures. Specifically, the gridding size is reduced from 15 to 10 pixels and from 10 to 5 pixels in the second and third iteration steps, respectively, to obtain a refined DVF motion pattern.

2.2 RC-4DMRF experiment

The MRF fast acquisition with steady-state precession (MRF-FISP) sequence was utilized for MRF data acquisition in RC-4DMRF experiments [26, 28], which were performed on digital human phantoms and on *in vivo* patients diagnosed with liver cancer.

2.2.1 MRF sequence

The MRF-FISP sequence employs an inversion recovery pulse with an inversion time (TI) of 18 ms, followed by 1,000 consecutive radiofrequency (RF) pulses with an echo time (TE) of 1.77 ms. The FAs and TRs are designed with a "half-sine" style, ranging from 0° to 70° and 11.7 to 14.3 ms, respectively. The MRF-FISP sequence acquires *k*-space data using a 2D spiral readout trajectory in the sagittal plane, which is repeated in the medial-lateral (ML) direction to cover the volumes of interest (VOIs) with a slice thickness of 5 mm. Additional MRF-FISP sequence parameters include an in-plane resolution of 256 × 256, a field of view (FOV) of 300 × 300 mm^2, and a scan time of 13 s per slice. An MRF dictionary comprising 8,000 elements was simulated using the extended phase graph algorithm [20] based on the MRF-FISP parameters. The dictionary includes T1 relaxation times ranging from 10 to 4,000 ms and T2 relaxation times ranging from 10 to 1,000 ms.

2.2.2 Digital human phantom experiment

A digital human phantom experiment was performed on 10 whole-body motion phantoms simulated by the extended cardiac-torso phantom [29-31]. The T1, T2, and PD values of multiple organs (e.g., the liver, tumor, and kidney) were determined according to *in vivo* measurements obtained in a 3T scanner [32, 33] (see **Appendix 1**). The 10 motion phantoms were characterized by unique irregular breathing patterns, each with a maximum diaphragm motion of 2.0 cm in the superior-inferior (SI) direction and 1.2 cm in the anterior-posterior (AP) direction. The numerical

k-space data were simulated by the extended phase graph algorithm and NUFFT algorithm based on the MRF sequence parameters in **Section 2.2.1** [20, 34].

2.2.3 *In vivo* patient experiment

A cohort of 13 patients with hepatocellular carcinoma (HCC) was enrolled for the *in vivo* patient experiment, consisting of three female patients (mean age: 64.7 ± 1.2 years) and ten male patients (mean age: 58.9 ± 8.7 years). The study protocol was approved by the institutional review board. Free-breathing MRF scans were conducted using a 3T scanner (SIGNA Premier, GE Healthcare) and 50 body coils were utilized for signal reception. VOIs were determined based on the planning target volume (PTV) and the number of sagittal slices varied from 10 to 20, depending on the length of the PTV in the ML direction. All patients underwent routine clinical computed tomography (CT) and contrast-enhanced magnetic resonance imaging (CE-MRI) scans for RT treatment planning. Besides, a cine MRI scan was performed on each patient, after MRF scans, for measurement of tumor motion.

2.3 Evaluation metrics

The fidelity of RC-4DMRF was assessed using three evaluation metrics: motion measurement accuracy, tissue quantification accuracy, and tumor-to-liver contrast. All of the statistical results were reported by the mean value with variability measured in standard deviation (mean ± standard deviation). The statistical significance of the results was ascertained through the application of a paired Student's t-test, and a p-value of less than 0.05 was considered statistically significant.

Motion measurement accuracy was quantified by measuring inter-phase tumor motion trajectories. The localization of tumors was performed manually on the T1 map for each phase,

and the trajectories of tumor motion were calculated in both SI and AP directions [35]. The motion trajectory of the tumor as observed in cine MRI served as the reference. To minimize variation in respiratory motion across different breathing cycles, an average cine MRI method was employed to derive the average breathing pattern of the patient. This involved sorting the real-time cine MRI images into eight phases based on the respiratory signal and then reconstructing averaged cine MRI images that contained only a single breathing cycle [7, 36]. Amplitude motion differences (AMDs) and Pearson correlation coefficients (PCCs) were used as metrics to determine the level of agreement between the motion trajectories obtained by RC-4DMRF and those derived from the averaged cine MRI.

Tissue quantification accuracy was assessed by comparing the RC-4DMRF-derived T1, T2, and PD maps with their corresponding ground-truth maps in the digital human phantom experiment, as well as by comparing the measured tissue values with the reference values in the *in vivo* experiment. The VOIs in the digital human phantom experiment were liver, tumor, and total body area. The mean absolute percentage errors (MAPEs) of the VOIs for the eight-phase tissue maps were calculated using **Equation (3)**,

$$MAPE = \frac{100\%}{n}\sum_{i=1}^{n}\left|\frac{P_i - T_i}{T_i}\right| \quad (3)$$

where n is the total number of voxels in the VOIs, and P and T are the predicted and ground-truth VOI, respectively. The tissue quantification accuracy of RC-4DMRF was compared with that of other state-of-the-art baseline methods, namely, the methods of Li *et al*. [11], Cruz *et al*. [14], and Cao *et al*. [15]. As the method of Li *et al*. [11] uses 10 MRF scan repetitions (denoted a “10 rep” setting) and the other methods use only one MRF scan (denoted a “1 rep” setting), the results of both 1 rep and 10 rep settings for the method of Li *et al*. are reported to enable a fair between-

method comparison. In the *in vivo* patient experiment, the T1 and T2 values of multiple tissue types (tumor, liver, muscle, fat, and kidney) were measured and compared with reference values retrieved from previous quantitative MRI studies [32, 33].

The tumor-to-liver contrast was evaluated by determining the contrast-to-noise ratio (CNR) within the patient cohort. The regions of interest (ROIs) utilized for the CNR computation were identified based on the gross target volume (GTV) derived from the RT treatment planning CT. The tumor-to-liver CNR of RC-4DMRF was compared with those of the planning CT and CE-MRI scans.

3 Results

3.1 Motion measurement accuracy

RC-4DMRF demonstrated a high capability to accurately resolve respiratory motion and characterize liver motion patterns. The results of a representative patient are shown in **Figure 2**. The T1, T2, and PD maps of eight respiratory phases derived from RC-4DMRF are presented in sagittal planes (**Figure 2(a)**), transverse planes (**Figure 2(b)**), and coronal planes (**Figure 2(c)**), respectively. The lung-liver boundaries were clearly reconstructed at each phase, and the tumor and normal tissue had clear discriminations. The cine MRI images acquired in the corresponding motion phases are shown in **Figure 2(a)**. The tissue maps demonstrated respiratory motion similar to that seen in cine MRI. An animation of respiratory motion obtained from RC-4DMRF and cine MRI is shown in **Appendix 2**. **Figure 2(d)** demonstrates the tumor motion trajectories of the presented patient. The trajectories measured in RC-4DMRF yielded similar amplitude and motion patterns to those measured in cine MRI.

Amongst all the patients, the average AMD between RC-4DMRF and cine MRI was 1.48 ± 1.06 mm in the SI direction and 0.81 ± 0.64 mm in the AP direction, and the average PCC between RC-4DMRF and cine MRI was 0.95 ± 0.05 in the SI direction and 0.93 ± 0.09 in the AP direction.

3.2 Tissue quantification accuracy

RC-4DMRF also achieved high accuracy in tissue property quantification. **Figure 3** demonstrates the results of the digital human phantom experiment. The error maps show minimal tissue property quantification errors (a narrow color window is used in error maps for better visualization of error regions). **Appendix 3** presents the animation of respiratory motion obtained by RC-4DMRF and the corresponding ground truth. The MAPEs of VOIs in the T1, T2, and PD maps generated by RC-4DMRF and other reconstruction methods are presented in **Table 1**. RC-4DMRF achieved the lowest MAPE for all VOIs (all p-values < 0.05). Among different tissue properties, the lowest MAPE was achieved in PD, whereas the highest MAPE was found in T2. **Table 2** lists the T1 and T2 values of different organs obtained in the *in vivo* patient experiment, as well as the corresponding reference values. The measured values are in good agreement with the reference values. In particular, the measured T1 values demonstrate higher correlation than T2 values.

3.3 Tumor-to-liver contrast

A comparison of the RC-4DMRF tissue maps with clinical scans (CE-MRI and planning CT scans) is shown in **Figure 4**. The average tumor-to-liver CNRs in the T1, T2, and PD maps were 7.27 ± 2.06, 3.81 ± 5.52, and 3.20 ± 4.62, respectively, and those in the CE-MRI and planning CT scans were 6.96 ± 1.01 and 2.91 ± 1.97, respectively. Among different quantitative tissue maps,

the T1 map had the highest tumor contrast; it was significantly greater than that of the planning CT scan (p-value = 0.048) and was comparable with that of the CE-MRI scan (p-value = 0.862). In addition, as shown in the expanded images, the T1 map demonstrated clearer tumor boundaries than the CE-MRI scan.

4 Discussion

This study has successfully developed a novel technique, RC-4DMRF, for improving the management of tumor motion in liver cancer RT. To the best of our knowledge, this is the first investigation to explore the feasibility of using 4DMRF for imaging liver cancer patients. The superiority and robustness of RC-4DMRF were verified through experiments on digital human phantoms and 13 patients with HCC, respectively. RC-4DMRF attained voxel-level precision in measuring respiratory motion with high temporal resolution, demonstrated superior performance in tissue property quantification compared to state-of-the-art baseline methods [11-15], and exhibited excellent tumor-to-liver CNRs compared to those achievable with standard clinical scanning methods (planning CT and CE-MRI). These promising results lay a solid foundation for the application of RC-4DMRF for tumor motion management in liver cancer RT, including precise target volume determination and inter-fraction motion assessment. Moreover, RC-4DMRF could be effectively integrated into magnetic resonance-linear accelerator (MR-LINAC) for online adaptive RT, given that successful implementation of MRF has already been demonstrated in both 1.5T and 0.35T MR-LINAC [37, 38]. Ultimately, the use of RC-4DMRF has the potential to enhance the precision of radiation dose coverage for tumor eradication and alleviate the liver toxicity profile for normal function preservation.

RC-4DMRF successfully generates motion-free tissue property maps across eight respiratory phases with accurate motion measurement and consistent contrast. Respiratory motion

was resolved from free-breathing *k*-space raw data, which enabled clear visualization of diaphragm positions and tumor boundaries in the tissue maps. The tumor motion trajectories measured by RC-4DMRF were in excellent agreement with those obtained from cine MRI (PCC > 0.9). The AMDs in both SI and AP directions were approximately to the length of one pixel, and the trajectories gave rise to a higher AMD in the SI direction than in the AP direction. In this study, the 2D MRF-FISP sequence was used as the base sequence for 4DMRF acquisition because of its rapid *k*-space data acquisition speed (~13 s per slice), which provided higher temporal resolution in retrospective phase sorting compared to the 3D sequence. Volumetric MRF tissue maps were generated by sequentially acquiring multiple sagittal planes to cover the entire VOI. The T1 and T2 tissue maps of the coronal and transverse planes demonstrated consistent in-plane contrast, owing to the quantitative nature of MRF acquisition. In contrast, conventional multi-slice 4DMRI may exhibit inconsistent in-plane contrast if two slices are acquired at different times.

The RC-4DMRF method demonstrated the highest accuracy in tissue property quantification than other comparing 4DMRF methods. Moreover, the motion compensation design of RC-4DMRF resulted in its scan time being 90% shorter than that in the method of Li *et al*. The RC-4DMRF only requires one MRF scan (1,000 dynamics; ~13 s per slice) to reconstruct accurate tissue maps. In contrast, the method of Li *et al*. requires nine more scan repetitions (10,000 dynamics; ~3 mins per slice) to achieve accurate tissue maps and has the lowest performance when data from only 1 repetition are used. The lengthy acquisition time of the method proposed by Li *et al*. could be burdensome for patients during scanning and is inefficient in clinical practice. Among the three MC-based methods, the method of Cao *et al*. has a higher mapping error than that of Cruz *et al*. and RC-4DMRF, which may be attributable to the low accuracy of Demons registration [39]. RC-4DMRF employs the same registration algorithm as the method of Cruz *et al*. in the initial

inter-phase motion estimation step. However, the pyramid motion-compensation design of the RC-4DMRF updates the inter-phase motion during optimization, thereby reducing motion errors and improving the accuracy of tissue mapping.

The RC-4DMRF T1 maps showed tumor contrast comparable to that of CE-MRI scans. It is worth noting that RC-4DMRF tissue maps were obtained without the use of contrast agent. As the high intensity of the T1 maps might be due to micro-structural changes in the tumor regions, such quantitative tissue maps could be used for assessing intra-tumoral heterogeneity and longitudinal tumor response. CE-MRI scans were obtained in free-breathing mode in the clinic, resulting in images with blurred tumor boundaries. In contrast, motion-resolved RC-4DMRF T1 maps had sharp tumor boundaries, which could improve the accuracy of GTV determination. A comparison of the three quantitative maps (T1, T2, and PD) from RC-4DMRF revealed significantly lower tumor contrast in T2 and PD maps than in T1 maps. Nevertheless, co-registered T2 and PD maps can provide additional anatomical information for tumor determination. For instance, both the tumor and vessels exhibited high intensity in the T1 map of Patient B (**Figure 4**), whereas only the vessels exhibited high intensity in the PD map. Therefore, combining the T1 and PD maps could precisely determine the tumor region. Overall, quantitative 4D tissue maps might present superior advantages over CE-MRI scans in determining target volume, owing to the simultaneous assessment of tumor regions and their motion ranges, which cannot be practically achieved by CE-MRI scans.

There are several future directions to explore for enhancing the performance of RC-4DMRF. Firstly, the development of a more efficient RC-4DMRF approach is warranted given the time-consuming nature of the current iterative-based method, which on average takes 18 minutes to reconstruct tissue maps for one slice and up to 180-360 minutes to reconstruct a 4D

volume depending on the patient's imaging volume. The utilization of deep learning techniques, such as deep learning-based low-rank NUFFT [40, 41] and deep learning-based inter-phase motion estimation [42], may significantly decrease the reconstruction time and should be considered for future investigation. Secondly, despite being the first study of its kind to evaluate the use of 4DMRF for imaging liver cancer patients, a more comprehensive clinical evaluation of RC-4DMRF is necessary. Specifically, the accuracy of internal target volume (ITV) determination, a crucial step in motion management and treatment planning, needs to be assessed and compared to those generated from 4DCT and 4DMRI. Finally, a dosimetric evaluation of the treatment plan would be valuable in assessing the clinical benefits of RC-4DMRF in terms of tumor control and preservation of normal liver tissue. While this aspect is beyond the scope of the present study, it presents an exciting avenue for future research.

5 Conclusions

RC-4DMRF has been successfully developed and validated in a prospective cohort of liver cancer patients, demonstrating high accuracy in simultaneous respiratory motion measurement and tissue property quantification. This novel 4D imaging technique holds great promise in improving the motion management of liver cancer RT. Further clinical investigations in aspects of target determination and dosimetry will be of great interest when it comes to contextualizing the applicability of RC-4DMRF. Ultimately, the use of RC-4DMRF may improve the treatment outcomes of countless liver cancer sufferers around the world by strengthening radiation dose coverage for tumor eradication and mitigating the risk of unnecessary radiation-induced liver complications.

Reference

[1] H. Sung *et al.*, "Global Cancer Statistics 2020: GLOBOCAN Estimates of Incidence and Mortality Worldwide for 36 Cancers in 185 Countries," *CA: A Cancer Journal for Clinicians,* vol. 71, no. 3, pp. 209-249, 2021, doi: https://doi.org/10.3322/caac.21660.

[2] S. R. Horn *et al.*, "Epidemiology of liver metastases," *Cancer Epidemiol,* vol. 67, p. 101760, Aug 2020, doi: 10.1016/j.canep.2020.101760.

[3] S. C. Davies, A. L. Hill, R. B. Holmes, M. Halliwell, and P. C. Jackson, "Ultrasound quantitation of respiratory organ motion in the upper abdomen," *Br J Radiol,* vol. 67, no. 803, pp. 1096-102, Nov 1994, doi: 10.1259/0007-1285-67-803-1096.

[4] G. Harauz and M. J. Bronskill, "Comparison of the liver's respiratory motion in the supine and upright positions: concise communication," *J Nucl Med,* vol. 20, no. 7, pp. 733-5, Jul 1979.

[5] F. D. Lasley *et al.*, "Treatment variables related to liver toxicity in patients with hepatocellular carcinoma, Child-Pugh class A and B enrolled in a phase 1-2 trial of stereotactic body radiation therapy," *Pract Radiat Oncol,* vol. 5, no. 5, pp. e443-e449, Sep-Oct 2015, doi: 10.1016/j.prro.2015.02.007.

[6] Y. Liu, F. F. Yin, B. G. Czito, M. R. Bashir, and J. Cai, "T2-weighted four dimensional magnetic resonance imaging with result-driven phase sorting," *Med Phys,* vol. 42, no. 8, pp. 4460-71, Aug 2015, doi: 10.1118/1.4923168.

[7] W. Harris, F. F. Yin, C. Wang, Y. Zhang, J. Cai, and L. Ren, "Accelerating volumetric cine MRI (VC-MRI) using undersampling for real-time 3D target localization/tracking in radiation therapy: a feasibility study," *Phys Med Biol,* vol. 63, no. 1, p. 01nt01, Dec 14 2017, doi: 10.1088/1361-6560/aa9746.

[8] E. Subashi *et al.*, "View-sharing for 4D magnetic resonance imaging with randomized projection-encoding enables improvements of respiratory motion imaging for treatment planning in abdominothoracic radiotherapy," *Physics and Imaging in Radiation Oncology,* vol. 25, p. 100409, 2023/01/01/ 2023, doi: https://doi.org/10.1016/j.phro.2022.12.006.

[9] H. Xiao *et al.*, "A dual-supervised deformation estimation model (DDEM) for constructing ultra-quality 4D-MRI based on a commercial low-quality 4D-MRI for liver cancer radiation therapy," *Med Phys,* vol. 49, no. 5, pp. 3159-3170, May 2022, doi: 10.1002/mp.15542.

[10] L. Zhang *et al.*, "Multi-contrast four-dimensional magnetic resonance imaging (MC-4D-MRI): Development and initial evaluation in liver tumor patients," *Medical Physics,* vol. 48, no. 12, pp. 7984-7997, 2021, doi: https://doi.org/10.1002/mp.15314.

[11] T. Li, D. Cui, E. S. Hui, and J. Cai, "Time-resolved magnetic resonance fingerprinting for radiotherapy motion management," *Medical Physics,* vol. 47, no. 12, pp. 6286-6293, 2020, doi: https://doi.org/10.1002/mp.14513.

[12] T. Li, D. Cui, G. Ren, E. S. Hui, and J. Cai, "Investigation of the effect of acquisition schemes on time-resolved magnetic resonance fingerprinting," *Phys Med Biol,* vol. 66, no. 9, Apr 28 2021, doi: 10.1088/1361-6560/abf51f.

[13] S. S. Huang, R. Boyacioglu, R. Bolding, C. MacAskill, Y. Chen, and M. A. Griswold, "Free-Breathing Abdominal Magnetic Resonance Fingerprinting Using a Pilot Tone Navigator," *Journal of Magnetic Resonance Imaging,* vol. 54, no. 4, pp. 1138-1151, 2021, doi: https://doi.org/10.1002/jmri.27673.

[14] G. Cruz *et al.*, "Generalized low-rank nonrigid motion-corrected reconstruction for MR fingerprinting," *Magnetic Resonance in Medicine,* vol. n/a, no. n/a, 2021, doi: https://doi.org/10.1002/mrm.29027.

[15] P. Cao, Z. Wang, C. Liu, T. Li, E. S. Hui, and J. Cai, "Motion-resolved and free-breathing liver MRF," *Magn Reson Imaging,* vol. 91, pp. 69-80, Sep 2022, doi: 10.1016/j.mri.2022.05.015.
[16] M. Davies, G. Puy, P. Vandergheynst, and Y. Wiaux, "A compressed sensing framework for magnetic resonance fingerprinting," *Siam journal on imaging sciences,* vol. 7, no. 4, pp. 2623-2656, 2014.
[17] J. Assländer, M. A. Cloos, F. Knoll, D. K. Sodickson, J. Hennig, and R. Lattanzi, "Low rank alternating direction method of multipliers reconstruction for MR fingerprinting," *Magnetic Resonance in Medicine,* vol. 79, no. 1, pp. 83-96, 2018, doi: https://doi.org/10.1002/mrm.26639.
[18] G. Mazor, L. Weizman, A. Tal, and Y. C. Eldar, "Low-rank magnetic resonance fingerprinting," *Medical Physics,* vol. 45, no. 9, pp. 4066-4084, 2018, doi: https://doi.org/10.1002/mp.13078.
[19] D. Ma *et al.*, "Magnetic resonance fingerprinting," *Nature,* vol. 495, no. 7440, pp. 187-192, 2013/03/01 2013, doi: 10.1038/nature11971.
[20] M. Weigel, "Extended phase graphs: dephasing, RF pulses, and echoes - pure and simple," *J Magn Reson Imaging,* vol. 41, no. 2, pp. 266-95, Feb 2015, doi: 10.1002/jmri.24619.
[21] D. F. McGivney *et al.*, "SVD compression for magnetic resonance fingerprinting in the time domain," *IEEE transactions on medical imaging,* vol. 33, no. 12, pp. 2311-2322, 2014, doi: 10.1109/TMI.2014.2337321.
[22] M. Lustig, D. Donoho, and J. M. Pauly, "Sparse MRI: The application of compressed sensing for rapid MR imaging," *Magnetic Resonance in Medicine,* vol. 58, no. 6, pp. 1182-1195, 2007, doi: https://doi.org/10.1002/mrm.21391.
[23] M. Modat *et al.*, "Fast free-form deformation using graphics processing units," *Computer Methods and Programs in Biomedicine,* vol. 98, no. 3, pp. 278-284, 2010/06/01/ 2010, doi: https://doi.org/10.1016/j.cmpb.2009.09.002.
[24] D. Rueckert, L. I. Sonoda, C. Hayes, D. L. G. Hill, M. O. Leach, and D. J. Hawkes, "Nonrigid registration using free-form deformations: application to breast MR images," *IEEE Transactions on Medical Imaging,* vol. 18, no. 8, pp. 712-721, 1999, doi: 10.1109/42.796284.
[25] J. Clayden, M. Modat, B. Presles, T. Anthopoulos, and P. Daga. "RNiftyReg: Image Registration Using the 'NiftyReg' Library." https://cran.r-project.org/web/packages/RNiftyReg/index.html (accessed.
[26] X. Cao *et al.*, "Robust sliding-window reconstruction for Accelerating the acquisition of MR fingerprinting," *Magnetic Resonance in Medicine,* vol. 78, no. 4, pp. 1579-1588, 2017, doi: https://doi.org/10.1002/mrm.26521.
[27] P. G. Batchelor, D. Atkinson, P. Irarrazaval, D. L. G. Hill, J. Hajnal, and D. Larkman, "Matrix description of general motion correction applied to multishot images," *Magnetic Resonance in Medicine,* vol. 54, no. 5, pp. 1273-1280, 2005, doi: https://doi.org/10.1002/mrm.20656.
[28] Y. Jiang, D. Ma, N. Seiberlich, V. Gulani, and M. A. Griswold, "MR fingerprinting using fast imaging with steady state precession (FISP) with spiral readout," *Magnetic Resonance in Medicine,* vol. 74, no. 6, pp. 1621-1631, 2015, doi: https://doi.org/10.1002/mrm.25559.
[29] W. P. Segars, G. Sturgeon, S. Mendonca, J. Grimes, and B. M. Tsui, "4D XCAT phantom for multimodality imaging research," *Med Phys,* vol. 37, no. 9, pp. 4902-15, Sep 2010, doi: 10.1118/1.3480985.
[30] R. K. Panta, P. Segars, F. F. Yin, and J. Cai, "Establishing a framework to implement 4D XCAT phantom for 4D radiotherapy research," *J Cancer Res Ther,* vol. 8, no. 4, pp. 565-70, Oct-Dec 2012, doi: 10.4103/0973-1482.106539.
[31] W. P. Segars, B. M. W. Tsui, C. Jing, Y. Fang-Fang, G. S. K. Fung, and E. Samei, "Application of the 4-D XCAT Phantoms in Biomedical Imaging and Beyond," *IEEE Trans Med Imaging,* vol. 37, no. 3, pp. 680-692, Mar 2018, doi: 10.1109/tmi.2017.2738448.

[32] J. Z. Bojorquez, S. Bricq, C. Acquitter, F. Brunotte, P. M. Walker, and A. Lalande, "What are normal relaxation times of tissues at 3 T?," *Magn Reson Imaging,* vol. 35, pp. 69-80, Jan 2017, doi: 10.1016/j.mri.2016.08.021.

[33] C. M. de Bazelaire, G. D. Duhamel, N. M. Rofsky, and D. C. Alsop, "MR imaging relaxation times of abdominal and pelvic tissues measured in vivo at 3.0 T: preliminary results," *Radiology,* vol. 230, no. 3, pp. 652-9, Mar 2004, doi: 10.1148/radiol.2303021331.

[34] J. A. Fessler and B. P. Sutton, "Nonuniform fast Fourier transforms using min-max interpolation," *IEEE Transactions on Signal Processing,* vol. 51, no. 2, pp. 560-574, 2003, doi: 10.1109/TSP.2002.807005.

[35] Y. Liu *et al.*, "Four-dimensional diffusion-weighted MR imaging (4D-DWI): a feasibility study," *Med Phys,* vol. 44, no. 2, pp. 397-406, Feb 2017, doi: 10.1002/mp.12037.

[36] J. Yang *et al.*, "Four-Dimensional Magnetic Resonance Imaging Using Axial Body Area as Respiratory Surrogate: Initial Patient Results," *International Journal of Radiation Oncology*Biology*Physics,* vol. 88, no. 4, pp. 907-912, 2014/03/15/ 2014, doi: https://doi.org/10.1016/j.ijrobp.2013.11.245.

[37] T. Bruijnen *et al.*, "Technical feasibility of magnetic resonance fingerprinting on a 1.5T MRI-linac," *Phys Med Biol,* vol. 65, no. 22, p. 22nt01, Nov 12 2020, doi: 10.1088/1361-6560/abbb9d.

[38] N. J. Mickevicius, J. P. Kim, J. Zhao, Z. S. Morris, N. J. Hurst Jr., and C. K. Glide-Hurst, "Toward magnetic resonance fingerprinting for low-field MR-guided radiation therapy," *Medical Physics,* vol. 48, no. 11, pp. 6930-6940, 2021, doi: https://doi.org/10.1002/mp.15202.

[39] X. Pennec, P. Cachier, and N. Ayache, "Understanding the “demon’s algorithm”: 3D non-rigid registration by gradient descent," in *International Conference on Medical Image Computing and Computer-Assisted Intervention*, 1999: Springer, pp. 597-605.

[40] M. Golbabaee *et al.*, "Compressive MRI quantification using convex spatiotemporal priors and deep encoder-decoder networks," *Medical image analysis,* vol. 69, p. 101945, 2021/04/01/ 2021, doi: https://doi.org/10.1016/j.media.2020.101945.

[41] C. Li, W. Li, C. Liu, H. Zheng, J. Cai, and S. Wang, "Artificial intelligence in multiparametric magnetic resonance imaging: A review," *Medical Physics,* vol. 49, no. 10, pp. e1024-e1054, 2022, doi: https://doi.org/10.1002/mp.15936.

[42] M. Hoffmann, B. Billot, D. N. Greve, J. E. Iglesias, B. Fischl, and A. V. Dalca, "SynthMorph: Learning Contrast-Invariant Registration Without Acquired Images," *IEEE Trans Med Imaging,* vol. 41, no. 3, pp. 543-558, Mar 2022, doi: 10.1109/tmi.2021.3116879.

List of Figures and Tables

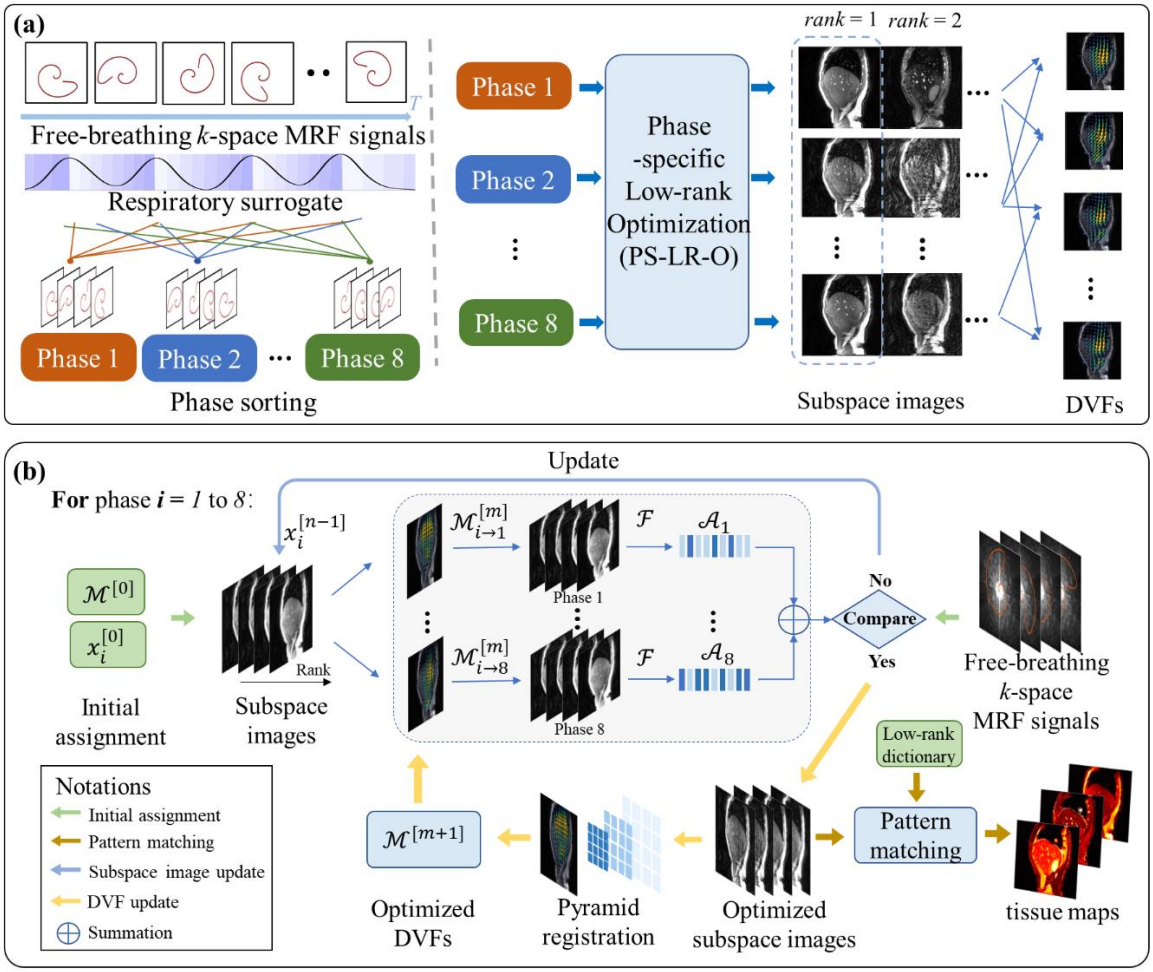

Figure 1. Schematic illustration of respiratory-correlated four-dimensional magnetic resonance fingerprinting (RC-4DMRF) **(a)** Initial inter-phase motion estimation. The inter-phase motion is estimated by projecting the phase-specific data onto a low-rank subspace. Specifically, the free-breathing MRF signals are first phase-sorted into different respiratory phases. The motion reference images are the *rank*-1 subspace images obtained by a phase-specific low-rank optimization (PS-LR-O) method. The deformation vector fields (DVFs) between every two motion phases are estimated using a free-form registration algorithm. **(b)** Pyramid motion-compensated optimization. The inter-phase DVFs ($\mathcal{M}$) and the phase-specific subspace images (x) are iteratively reconstructed with a total iteration step of three. The DVFs estimated in **(a)** are used as

the initial assignment in the reconstruction. At the end of the reconstruction, the optimized subspace images are used for pattern matching to obtain high-quality four-dimensional tissue maps.

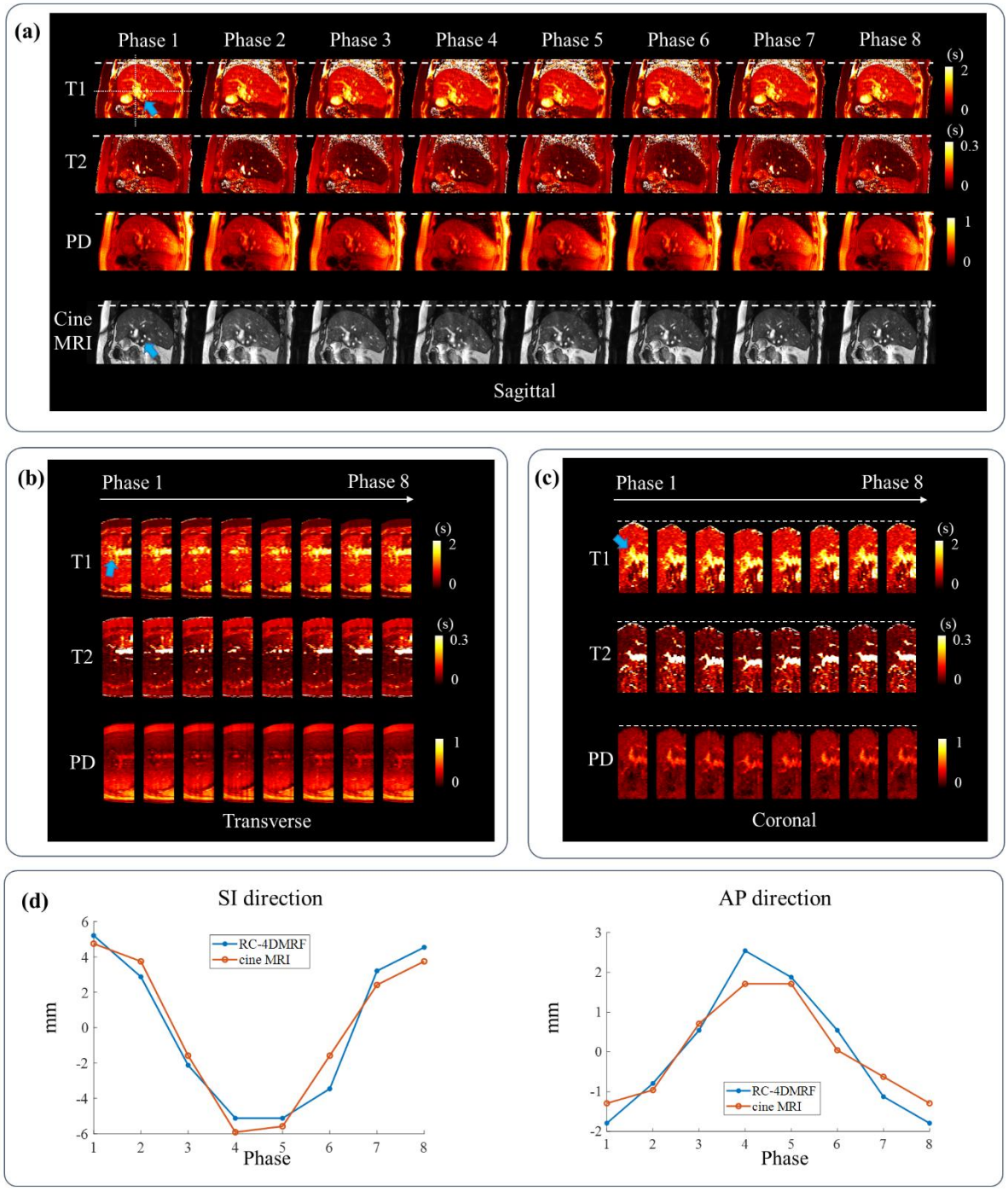

Figure 2. Respiratory-correlated four-dimensional magnetic resonance fingerprinting (RC-4DMRF) reconstruction result of a representative patient. T1, T2, and proton density (PD) tissue maps of eight respiratory phases are shown in the sagittal plane **(a)**, transverse plane **(b)**, and

coronal plane **(c)**, respectively. The locations of the transverse and coronal planes are indicated by the white dotted lines in **(a)** (T1 map, phase 1). The tumor is indicated by the blue arrows, and the white dashed lines are added to facilitate the visualization of diaphragm motion. The cine MRI images acquired in the corresponding motion phases are shown in the fourth row of **(a)**. In addition, the tumor motion trajectories of the presented patient in the superior-inferior (SI) and anterior-posterior (AP) directions are shown in **(d)**.

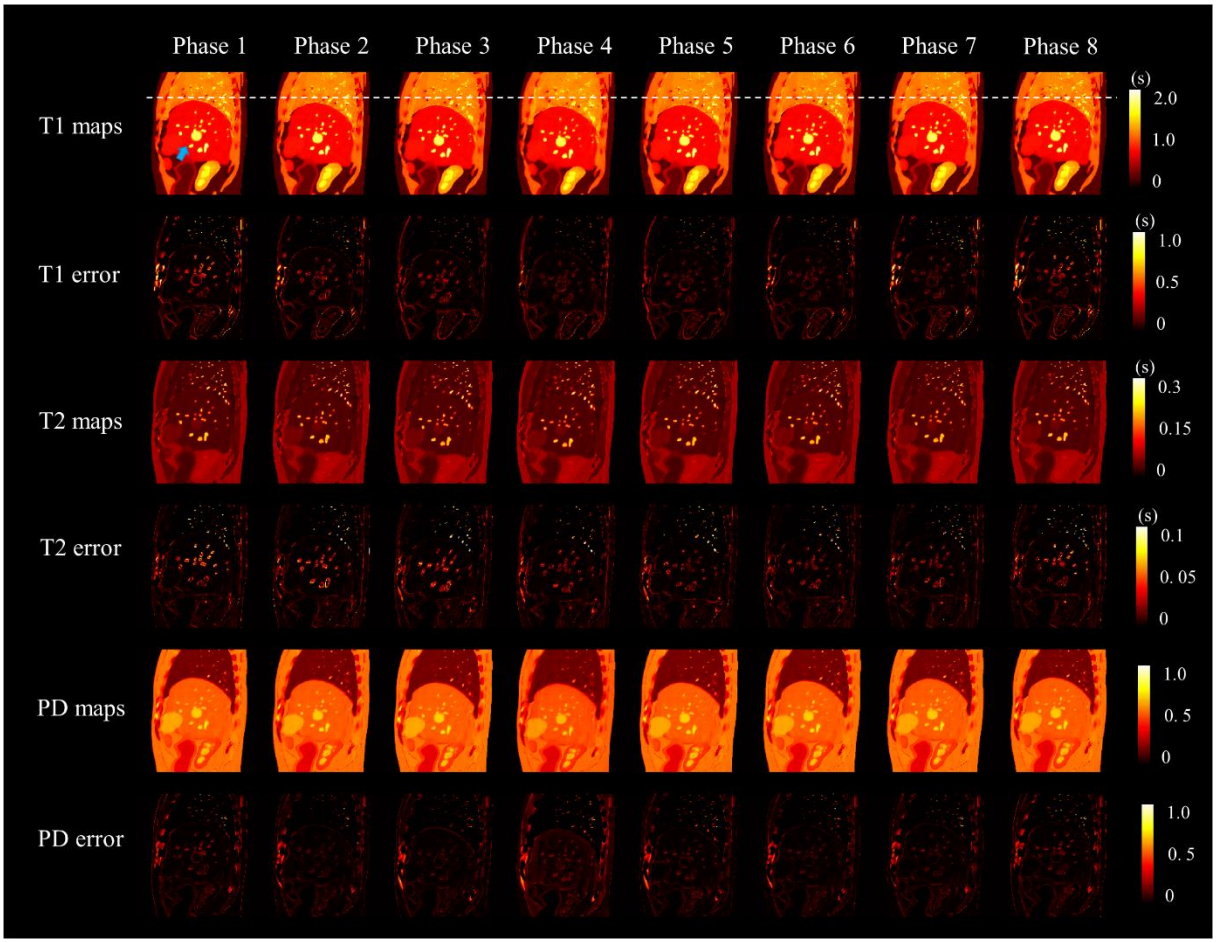

Figure 3. Respiratory-correlated four-dimensional magnetic resonance fingerprinting (RC-4DMRF) reconstruction result of a digital human phantom. T1, T2, and proton density (PD) tissue maps of eight respiratory phases are shown in the first, third, and fifth rows, and the corresponding absolute error maps are shown in the second, fourth, and sixth rows. The tumor is indicated by the blue arrow, and the white dashed lines are added to facilitate the visualization of diaphragm motion. The color window of the error maps is narrower compared to that of the tissue maps to improve the visualization of the error region. An animation of respiratory motion is given in **Appendix 3**.

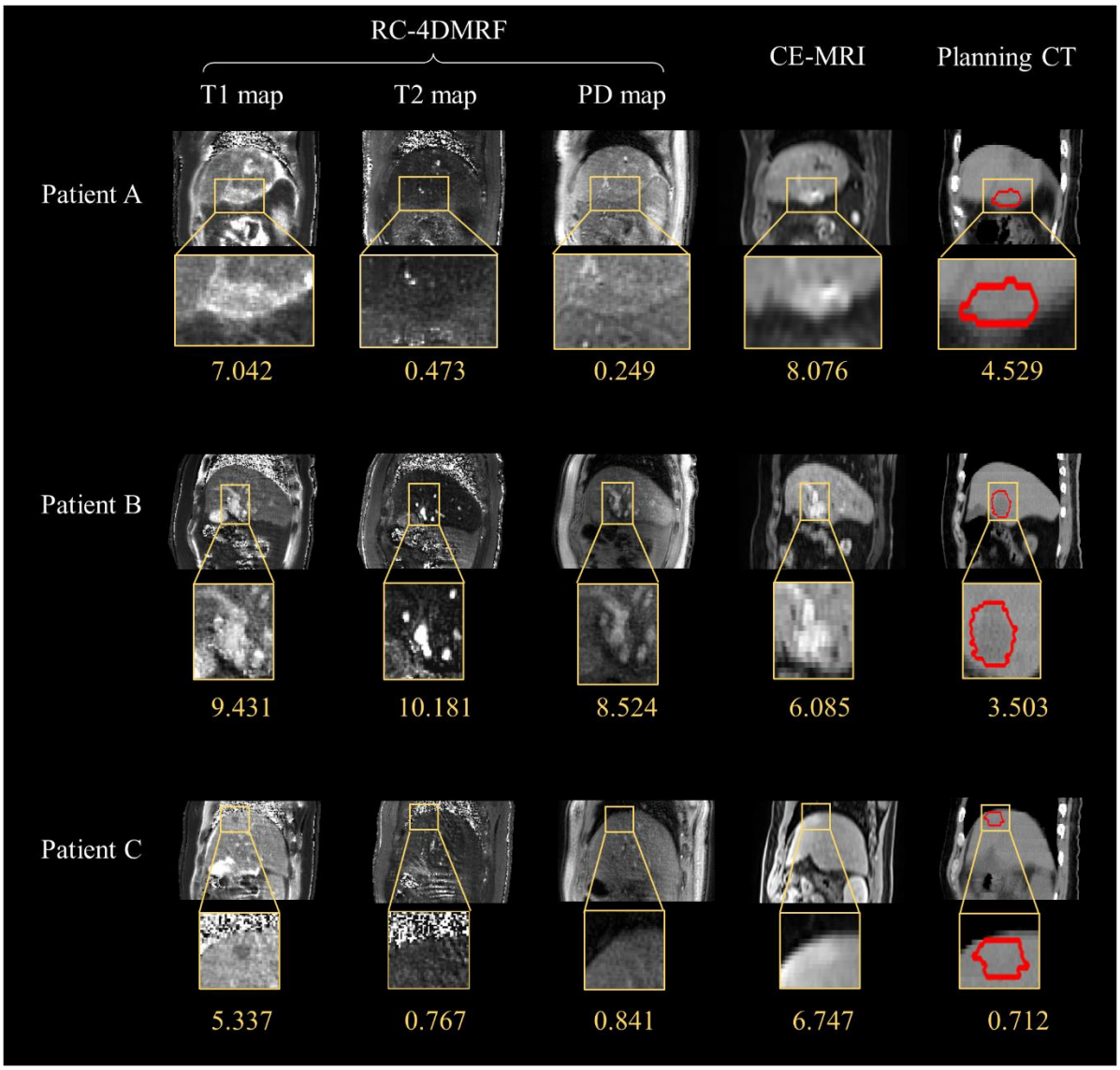

Figure 4. Comparison of respiratory-correlated four-dimensional magnetic resonance fingerprinting (RC-4DMRF) tissue maps with clinical scans (contrast-enhanced magnetic resonance imaging (CE-MRI) and planning computed tomography (CT) scans). The tumor regions are expanded in the yellow boxes, and the gross target volumes are contoured by the red lines in the CT images. The tumor contrast-to-noise ratio is presented under each yellow box.

Table 1. Results of quantitative evaluation of different reconstruction methods for the accuracy of tissue property quantification. The accuracy of respiratory-correlated four-dimensional magnetic resonance fingerprinting (RC-4DMRF) was compared with the accuracies of three other 4DMRF methods: those of Li *et al*. [15], Cruz *et al.* [18], and Cao *et al.* [19]. The evaluation was performed on digital human phantoms (n = 10). The results are reported as mean absolute percentage errors with variability measured in standard deviations (MAPEs ± SDs) for volumes of interest (VOIs) in the tumor, liver, and total phantom body region.

T1 MAPE ± SD (%)			
	Tumor	Liver	Total
Li *et al.* (1 rep) * [15]	70.91 ± 3.19	148.02 ± 13.56	149.25 ± 26.29
Li *et al.* (10 rep) * [15]	13.65 ± 2.07	19.38 ± 2.60	20.34 ± 1.86
Cao *et al*. [19]	14.40 ± 2.92	14.72 ± 1.99	16.83 ± 1.92
Cruz *et. al*. [18]	9.22 ± 2.73	9.53 ± 1.39	13.18 ± 1.73
RC-4DMRF	7.03 ± 2.88	4.67 ± 1.32	8.84 ± 1.63

T2 MAPE ± SD (%)			
	Tumor	Liver	Total
Li *et al.* (1 rep) * [15]	647.48 ± 195.72	937.72 ± 130.14	645.02 ± 55.30
Li *et al.* (10 rep) * [15]	16.93 ± 1.57	26.43 ± 2.19	25.03 ± 1.95
Cao *et al*. [19]	18.98 ± 3.77	33.70 ± 5.30	29.25 ± 3.68
Cruz *et. al*. [18]	10.58 ± 1.09	19.62 ± 9.48	20.64 ± 9.01
RC-4DMRF	4.61 ± 1.19	6.87 ± 1.44	9.65 ± 2.08

PD MAPE ± SD (%)			
	Tumor	Liver	Total
Li *et al.* (1 rep) * [15]	52.14 ± 4.24	65.69 ± 5.48	59.58 ± 6.34
Li *et al.* (10 rep) * [15]	12.11 ± 1.61	14.03 ± 1.38	11.60 ± 0.79
Cao *et al*. [19]	12.22 ± 1.49	12.44 ± 0.57	11.94 ± 0.24
Cruz *et. al*. [18]	6.81 ± 2.22	6.63 ± 0.62	7.01 ± 0.57
RC-4DMRF	4.54 ± 2.12	3.09 ± 0.68	5.00 ± 0.72

Abbreviations: PD = proton density

*“1 rep” indicates a result obtained from data acquired in a single MRF scan, whereas “10 rep” indicates a result obtained from data acquired in 10 repeated MRF scans.

Table 2. Quantitative results of the measured T1 and T2 relaxation time for multiple tissue types in an *in vivo* patient experiment. The measurement was performed on hepatocellular carcinoma (HCC) patients (n = 13) in a 3T scanner. The measured T1 and T2 values were compared with reference T1 and T2 values retrieved from previously published quantitative MRI studies [34, 35]. Results are reported as mean values in milliseconds (ms) with variability measured in standard deviations (Mean ± SD).

Organs	T1 Relaxation time (ms)			T2 Relaxation time (ms)		
	Measurement	Reference	Difference	Measurement	Reference	Difference
Liver	757 ± 78	809 ± 71	52	43 ± 13	34 ± 4	9
Fat	261 ± 53	253 ± 42	8	71 ± 11	68 ± 4	3
Muscle	1248 ± 70	1295 ± 83	47	55 ± 15	44 ± 9	11
Kidney (Cortex)	1453 ± 310	1314 ± 77	139	63 ±13	76 ± 7	13
Kidney (Medulla)	1863 ± 120	1702 ± 205	161	82 ± 15	81 ± 8	1
Tumor	1427 ± 435	N/A	N/A	208 ± 364	N/A	N/A

N/A: not applicable